Design and CFD performance analysis of a novel impeller for double suction centrifugal pumps

Design and CFD performance analysis of a novel impeller for double suction centrifugal pumps

T. Capurso[a], L. Bergamini[b], M. Torresi[a]

[a] *Polytechnic University of Bari, Via Edoardo Orabona, 4, 70126 Bari (Italy)*
[b] *Nuovo Pignone, Strada Provinciale Modugno Bari 10, 70123 Bari (Italy)*

Abstract

Double suction centrifugal pumps are the main devices involved in the feedwater system of nuclear power plants and they are responsible for a significant share of their energy consumption (by affecting the balance of both the gross and net electrical energy production), hence even an efficiency increase of only a few percentage points could be substantial in their economy. Herein a novel impeller designed for low-medium specific speed double suction centrifugal pumps ($n_q < 60$) is proposed showing an efficiency improvement with respect to conventional designs in the order of $1 - 2\%$ associated to a slip factor increase, secondary losses reduction and impeller outflow homogeneity improvement. The novel double suction impeller is characterized by a new arrangement of its flow channels, which come up alternately on the same circumferential exit even if they start from the two different sides. The flow field through the impeller is investigated via numerical simulations run by means of the open source CFD code OpenFOAM and its performance is compared against experimental results. The CFD model set-up, in terms of grid size and discretization schemes, has been previously assessed against results of consolidated CFX simulations on a conventional centrifugal pump.

Keywords: Double Suction Centrifugal Pump, Slip Factor, CFD, OpenFOAM, 3D-URANS, Energy saving

[☆] Fully documented templates are available in the elsarticle package on CTAN.

Email addresses: tommaso.capurso@poliba.it (T. Capurso), Lorenzo.Bergamini@bhge.com (L. Bergamini), marco.torresi@poliba.it (M. Torresi)

2010 MSC: 00-01, 99-00

1. Introduction

World's energy consumption is expected to rise 28% from 2015 to 2040 [1] in order to satisfy the demand associated with the increase in world's population and economy. According to a research conducted by the International Energy Agency [2, 3], currently, electric motors consume 46% of the electricity generated in the world and, depending on the industry, centrifugal pumps consume between 25% and 60% of a plant electrical motor energy [4] . For instance, the energy consumption due to centrifugal pumps with respect to electrical motor energy demand is 26% in chemical industry, 31% in pulp and paper industry and 59% in petroleum industry [4]. In the field of the energy production, centrifugal pumps are widely used in nuclear and steam power plants as main component of feedwater system (feedwater and primary pumps) and they are responsible for a significant energy absorption (e.g., up to 2% in Hualong One [5]) being directly driven by either steam engines or electrical motors [6]. Centrifugal pumps in EU use 120 $TWh/year$ of electricity [7]. Recent studies about Life Cycle Cost (LCC) of pumping system have shown that approximately 50% of the total LCC stems from the energy costs; furthermore, it has been pointed out that, among all the rotating devices in a process plant, centrifugal pumps typically have the best overall potential for energy savings [4]. Hence an efficiency increase of these machines even of only a few percentage points could be substantial in the economy of a power plant, especially today when all the governments, industrial companies and research groups have to pay attention on the environmental issues.

This work deals with low-medium specific speed double suction pumps and it describes a 1D design procedure coupled with computational fluid dynamics (CFD) with the purpose to improve the efficiency of their impellers with respect to conventional designs. Low-medium specific speed double suction impellers ($n_q < 60$) are chiefly used when medium-high hydraulic heads (40 m

$< H < 250\ m$) and low-medium flow rates ($Q < 2\ m^3/s$) are required.

Commonly, a double suction impeller is made of two single suction impellers in a back-to-back arrangement [8]; each of those having a lower specific speed number and a marked radial impeller shape. At low-medium specific speeds, in order to ensure higher values of the flow rate, a double suction impeller is preferred to a mixed axial-radial impeller with the same specific speed, the latter being more subject to the risk of cavitation. Furthermore, a double suction impeller is able to balance the axial hydraulic thrust resulting in a compact system.

The performance of a centrifugal pump is strongly affected by disparate sources of loss (performance degradation), e.g., fluid dynamic friction losses. Concerning the impeller, the above mentioned losses mainly depend on the shape of the vanes. Furthermore, slip depends on the number of blades of the impeller, which is finite, and on the pressure conditions acting on both pressure and suction sides of the blades [8].

Nowadays the research about centrifugal pumps is focused on both design of multi-objective algorithms for pump definition and geometry optimization in order to improve impeller efficiency (reducing losses and enlarging the operative range with both single-phase and cavitating flows) and to develop less time consuming design tools. The first field includes, e.g., multi-objective optimization method using a Simulation-Kriging model-Experiment (SKE) approach [9, 10]. The latter includes global optimization method based on Artificial Neural Network (ANN), Artificial Bee Colony (ABC) [11] and analytical models based on potential flow theory [12]. In addition, there are works that introduce new methodologies based on Energy Loss Models and Computational Fluid Dynamics (ELM/CFD) [13] and impeller geometry modifications with respect to the conventional ones. For instance, with this regard, J. Skrzypacz et al. [9] suggested the introduction of micro grooves, performed on the front and rear disks, for low specific speed impellers in order to reduce the hydraulic losses. The application of micro grooves, which work as additional blades, should increase the ability of the impeller to transmit power to the liquid, particularly in the region

of the boundary layer. Neverthelss, many works deal with experimental study of centrifugal pump under transient operating conditions involving shut-off [6] and gas entrainment conditions [14] in order to prevent over-loads which can induce damage and failure.

In line with the works concerning the geometry optimization, herein a new design procedure for double suction centrifugal pumps is described. This is based on the assumption that slip at the outlet of the impeller can be reduced by increasing the number of blades [8]. Indeed, in the past different impeller geometries have been proposed trying to increase the number of the blades along the circumferential direction at the outlet of the impeller in order to improve the efficiency of double suction pumps and to reduce secondary flows at part load [15, 16, 17, 18]. They show completely new blade arrangements with respect to the ones conventionally used. Nevertheless, these proposals lack of simplicity, do not introduce detailed descriptions of the channel shape and give no information about the flow velocity control inside the impeller channels [19, 20].

The new impeller design allows one to double the number of blades at the outlet of the impeller in a way that the channel outlets, coming from the two sides, are circumferentially arranged and therefore the flow guidance is increased. The basic idea behind the novel impeller is its compatibility with the housing of the conventional impeller. The channels not only intersect each other without interference but also have a specific cross sectional area distribution along the center line (c-line). As it will be shown, this results in an increase of the slip factor, which leads to a higher value of the hydraulic head with respect to a conventional configuration with the same impeller outlet diameter. Other results are a higher value of the hydraulic diameter (D_h) and a lower length of the channels (L), which allow a lower amount of losses inside the new channel, hence improving the hydraulic efficiency. This will be highlighted by evaluating the rotary stagnation pressure inside the channel.

The novel geometry, presented in this work, has been designed writing a specific 1D code and performing simplified (single channel) numerical simulations carried out by means of the commercial CFD code ANSYS Fluent®. Once

the preliminary design came to an end, the novel impeller has been investigated both numerically and experimentally. The entire centrifugal pump geometry has been modeled and investigated by means of the CFD open-source code OpenFOAM in order to validate the results previously obtained via single channel simulations and to evaluate the influence of the actual suction pipe and double volute on the overall performance.

Computational Fluid Dynamics (CFD) has an important role in predicting hydraulic turbomachinery performance and designing new impellers since it allows a reduction of both design costs and time. As shown by S. Shah [21] there are many possibilities to simulate hydraulic turbomachinery. Steady-state simulations are useful to extend the basic understanding of the flow, but unsteady simulations are needed in order to take into account the actual flow interaction between steady (diffusers or volutes) and rotating (impeller) parts.

The OpenFOAM usage for CFD calculations is widely growing nowadays because it is opensource and it can be easily parallelized. OpenFOAM is able to perform steady, but also unsteady simulations by using DNS (Direct Numerical Simulations), LES (Large Eddy Simulations) and RANS (Reynolds Averaged Navier-Stokes) approaches which are already available in OpenFOAM, but also by implementing hybrid methods, e.g., Detached Eddy Simulations, DES, and Partially Averaged Navier-Stokes, PANS. Furthermore, H. Nilsson [22] showed that OpenFOAM is able to reach good agreement with results obtained by commercial codes (e.g., CFX) for hydraulic turbomachinery, such as turbines, pumps and propellers.

Among the previously listed methods the RANS approach is the most common technique used to solve the flow field inside centrifugal pumps, but LES simulations are becoming more and more attractive especially when complex geometries and flow phenomena are involved [23]. In the last decade also the Immersed Boundary Method (IBM) [24] becomes more popular. It has been applied to simulate centrifugal pumps [25] and it has been implemented in OpenFOAM as shown by M. Specklin et al. [26]. This method allows one to handle multi-phase flows or fluid-structure interaction problems, in a single-phase framework. One

of the main interests in IBM lies in the simplification of the model and especially in its suitability for use with Cartesian meshes of perfect orthogonal quality.

In this work the RANS method has been used because it is less time consuming compared to methods which require more detailed and finer grids and it is appropriate to get a reasonable estimation of the general performance of the centrifugal pump, from an engineering point of view, with typical errors below 10 percent compared with experimental data [21].

The paper is organized as follows: the design process and the reasons behind it are explained in paragraph 2. The numerical model and its set up are presented in the third part with a focus on the boundary conditions. Furthermore, a comparison of the numerical results obtained with OpenFOAM and CFX (performed by a different team of Nuovo Pignone) in the case of a conventional geometry is shown for validation (Fig.6). Finally, the numerical results for the novel geometry are presented in terms of ψ-ϕ (Fig.10) and hydraulic efficiency (Fig. 11) and compared against the results obtained for the conventional double suction pump. Moreover, velocity and vorticity contours at the outlet of the two impellers are shown in order to point out the benefits to using the novel impeller.

2. Design of the novel impeller geometry

The new double suction impeller is supposed to be used in substitution of a conventional one, defined as baseline, whose characteristic curve in non-dimensional form is shown in Fig.1.

The pump specific speed (n_q), defined as follows:

$$n_q = n\frac{\sqrt{Q_{BEP}/f_q}}{H_{BEP}^{0.75}} \tag{1}$$

is equal to 21.3. In eq.1, n is the rotational speed (rpm), Q is the volumetric flow rate (m^3/s), f_q is the number of impeller entries ($f_q = 2$ for a double suction one), H is the hydraulic head (m) and BEP stands for the Best Efficiency Point.

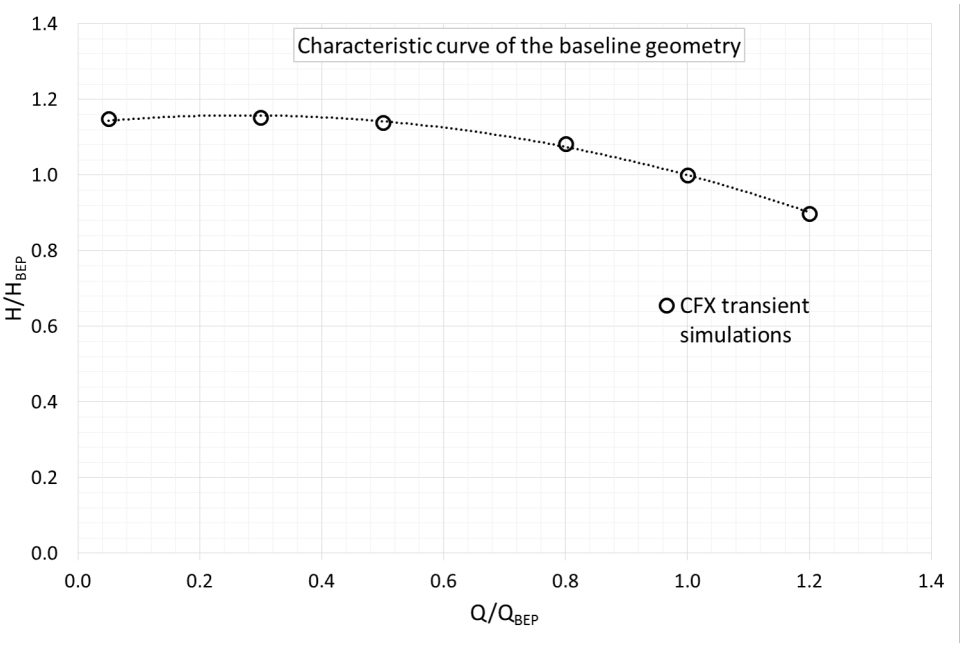

Figure 1: Characteristic curve (H/H_{BEP} - Q/Q_{BEP}) of a conventional double suction impeller obtained by means of transient CFX simulations during the design procedure (Grid size $\cong$ 40 million cells). Simulations performed by Nuovo Pignone.

In the next paragraphs, the comparison between different machines will be performed by means of two dimensionless parameters, namely the head coefficient, which is equal to:

$$\psi = \frac{2gH}{u_2^2} \tag{2}$$

the flow coefficient, which is defined as follows:

$$\varphi = \frac{Q}{\pi D_2^2 u_2/4} \tag{3}$$

In eq.3 and 2, D_2 is the outer diameter of the impeller, $u_2 = \pi D_2 n/60$ is the tangential velocity calculated at the outer diameter and g is the standard gravity. Furthermore, the global efficiency of these machine has been calculated as follows:

$$\eta = \frac{\rho g H Q}{C\omega} = \frac{Q\Delta P_{tot}}{C\omega} \tag{4}$$

where ΔP_{tot} is the total pressure difference between two flanges downstream and upstream the impeller (N/m^2), ρ is the density of the fluid (kg/m^3), ω is the angular velocity (rad/s) and C is the torque (Nm) exchanged by the fluid and the impeller, including the shear stress acting on the internal and external surfaces of the impeller (disk friction losses). These parameters allow one to compare the performance of various centrifugal pumps, regardless their dimensions and operating conditions.

2.1. Embodiments of the new impeller

The novel impeller is characterized by having the channels between the blades starting from either inlets, crossing the simmetry plane, normal to the rotational axis, and ending in such a way that the equivalent blades number at the impeller outlet is actually doubled with respect to a conventional configuration obtained by the back-to-back coupling of two single suction impellers (Fig.9). In the novel impeller, the slip reduction is supposed to occur due to the actual doubling of the number of blades at the impeller outlet, which permits the reduction of the impeller outer diameter, thus reducing the size and therefore the manufacturing cost of the pump. Furthermore, the reduction of the impeller diameter brings also along a significant reduction of the losses due to disk friction, thus increasing the overall pump efficiency.

Compared to a conventional double suction impeller provided with splitter blades, embodiments of the new impeller do not introduce any additional leading edge and corresponding losses [8]. For low-medium specific speed pumps, the new shape of the inter-blade channels of the impeller is such that the cross section hydraulic diameter is increased and the length of each channel reduced, thus reducing the hydraulic losses with respect to conventional configurations. The cross section area of the channel is designed to have control over the velocity of the flow inside the channel. Moreover, its shape is designed in order to avoid any channel interpenetration when they twist from the axial to the radial direction and at the same time to match a target area law (continuous in its first and second order derivative) along the flow path, in order to avoid too

high velocity gradients inside the channels. This leads to higher performance in terms of hydraulic head and global efficiency compared to other solutions, e.g., [19] and [20]. In particular, the channels start essentially with a four-sided polygonal cross-section which becomes a five sided polygon. When the channels become parallel to the radial tangential plane, their cross-sections return to be essentially quadrilateral. The additional side is introduced between the so called suction side and the hub surfaces of the channel. Its length starts from zero, reaches its maximum at about half of the channel length, and then goes back to zero. This novel channel geometry (Fig.9) is covered by a patent application in which further information about the geometry design can be found [27].

2.2. Design process and constraints

The stator parts, which are shown in Fig.2, represent design constraints to the outer diameter and the axial size according to which the new impeller has been designed together with other three important restrictions to be satisfied:

- to preserve the same specific speed number (n_q) of the baseline geometry;
- to guarantee at the Best Efficiency Point (BEP) a kinematic flow angle at the inlet of the volute (α_3) in accordance with the optimum α_3 of the volute (there is no bladed diffuser);
- to satisfy the matching of the relative inlet flow angle with the inlet geometric angle of the impeller.

The design of the new double suction impeller has been developed by writing a specific 1D code. In Figure 3 the design process is described in detail.

Initially, the code empirically estimates the slip factor, the hydraulic efficiency and the losses between the outer diameter and the volute inlet. After that the geometry is generated and simulations are then run on a single blade channel in order to define the correct value of the flow angles and fluid dynamics parameters, see Fig.4.

The computational domain, adopted for these calculations, comprises a short

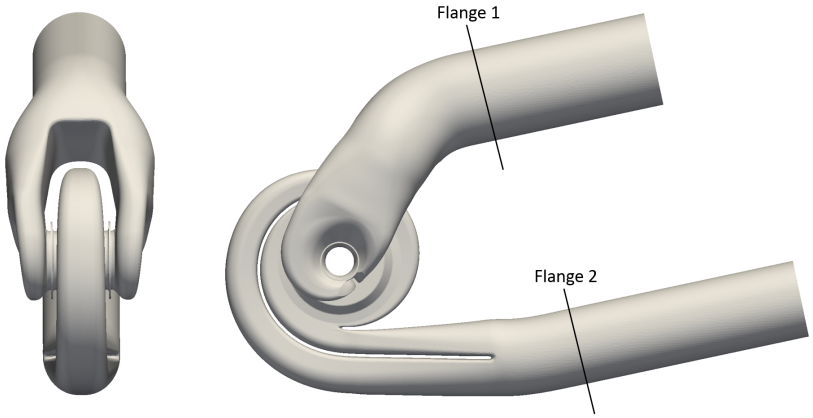

Figure 2: Front and side views of the model, which includes the inlet duct, the impeller and the double volute.

pipe upstream the blade channel inlet and a vaneless diffuser downstream the channel outlet with the aim to reduce the influence of the boundary conditions, see Fig.4. All the grids have been generated with the same grid generation strategy by means of Icem CFD® and they are made of 1 million cells with $y^+ = 1$. The wall y^+ is defined as:

$$y^+ = \frac{yU_\tau}{\nu} \tag{5}$$

where y is the cell centroid distance to the nearest wall, ν is the local kinematic viscosity of the fluid and U_τ is the friction velocity:

$$U_\tau = \sqrt{\frac{\tau_w}{\rho}} \tag{6}$$

In eq.6 τ_w is the wall shear stress, defined as follows:

$$\tau_w = \mu \left(\frac{\partial u}{\partial y} \right)_{y=0} \tag{7}$$

where μ is the dynamic viscosity, u is the flow velocity parallel to the wall and y is the distance from the wall.

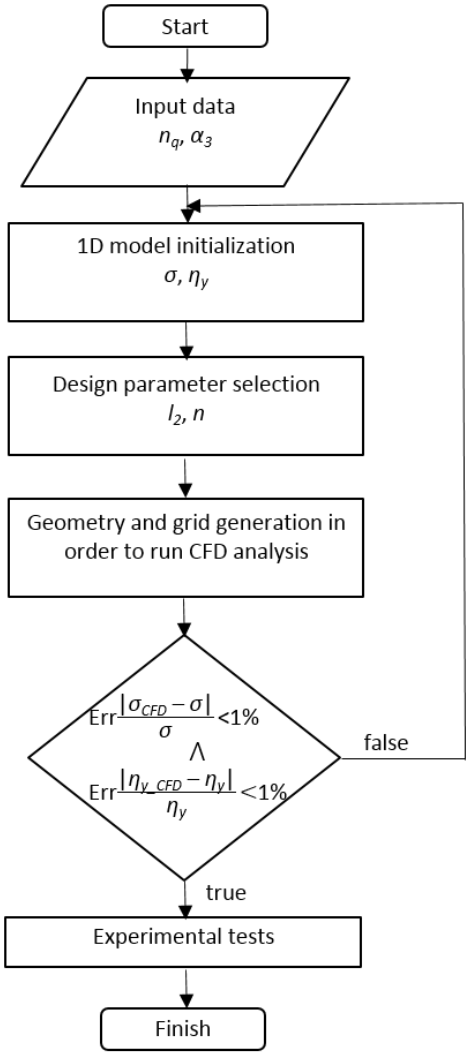

Figure 3: Flow chart of the design process.

CFD analyses have been run with the commercial code ANSYS Fluent® in steady state configuration by means of the Multiple Reference Frame (MRF) technique and the k-ω SST model for turbulence closure [28]. Regarding the boundary conditions, velocity components have been imposed at the inlet including the flow leakages (eq.9 and uniform pressure distribution at the outlet, whereas a constant turbulence intensity equal to 3% has been imposed at the

inlet. For all the simulations concerning the desing process the convection, diffusion and gradient terms have been computed by using second-order upwind schemes.

At the end of the numerical simulations the new values of losses and slip factor are then passed back to the 1D code. The process continues until convergence is reached, as summarized in Fig.3.

2.3. Slip factor enhancement

The slip factor is defined as follows:

$$\sigma = \frac{c_{u2}^{CFD}}{c_{u2}^{th}} \tag{8}$$

where c_{u2}^{CFD} is the absolute tangential velocity evaluated via area-weighted averages on surfaces placed at the exit of the impeller, whereas c_{u2}^{th} derives from the blade congruent flow theory. The hydraulic efficiency of the channel is calculated as:

$$\eta_y = \frac{Q' \Delta P_{tot}}{C\omega} \tag{9}$$

where ΔP_{tot} is the stagnation pressure difference between the inlet and the outlet of the channel (N/m^2), $Q' = Q/\eta_v$ is the volumetric flow rate (m^3/s) including the flow leakage, ω is the angular velocity (rad/s) and C is the torque calculated on the blade, the hub and the shroud (Nm).

As expected, the numerical results of the flow field concerning the novel geometry, obtained at the end of the convergence process, have shown an improvement in the slip factor (+8.5%) and in the hydraulic efficiency (+1.2%). The results obtained at the BEP of the two geometries are reported in Tab.1.

2.4. Rotary stagnation pressure evaluation

In order to quantify the energy loss, L_w, the rotary stagnation pressure drop, Δp^*, has been calculated inside the blade channel.

In a rotating system, the rotary stagnation pressure is defined as:

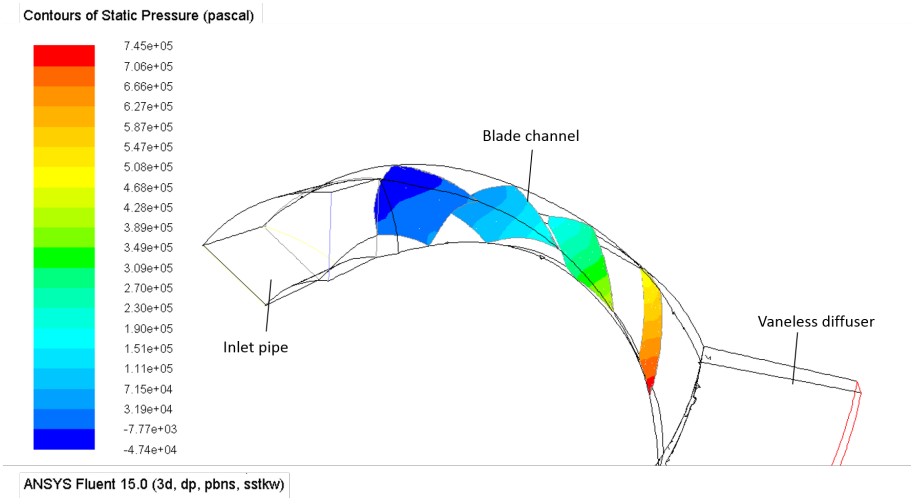

Figure 4: Description of the numerical domain and view of the static pressure contours inside the channel on iso-surfaces with constant meridional coordinate.

Table 1: Slip factor and hydraulic efficiency of the two geometries calculated at BEP via single vane simulations.

Tag name	Conventional	novel Geometry
hydraulic efficiency (η_y)	0.917	0.928 (+1.2%)
slip factor (σ)	0.782	0.854 (+8.5%)

$$-L_w = \frac{\Delta p^*}{\rho} = \Delta\left(\frac{p_{abs}}{\rho} + \frac{w^2}{2} - \frac{u^2}{2}\right) \tag{10}$$

where u is the local rotational speed defined as $u = \omega R$, p_{abs} is the absolute static pressure, and w is the relative velocity. For incompressible, inviscid flow, the value of p^* is constant along a streamline. For the viscous flow, the change of this parameter between two points on the same streamline represents the viscous loss.

The trend of the rotary stagnation pressure has been evaluated by means of area-weighted integrals on surfaces at constant meridional coordinates along the blade channel of the two geometries, i.e., the baseline and the novel one. Figure 5 points out that when the fluid flows through the baseline geometry it

is subjected to a more than linear reduction of the rotary stagnation pressure mainly in the first part (first 10%) and towards the outlet (last 40%) of the channel, whereas it experiences a linear reduction in the central part of the channel. On the contrary, the novel design shows a mild linear reduction of the rotary stagnation pressure along the entire channel length. This is due to the shape and reduced length of the novel channel: the new cross sections are more squared and have larger hydraulic diameters compared to the baseline decreasing the development of secondary flows.

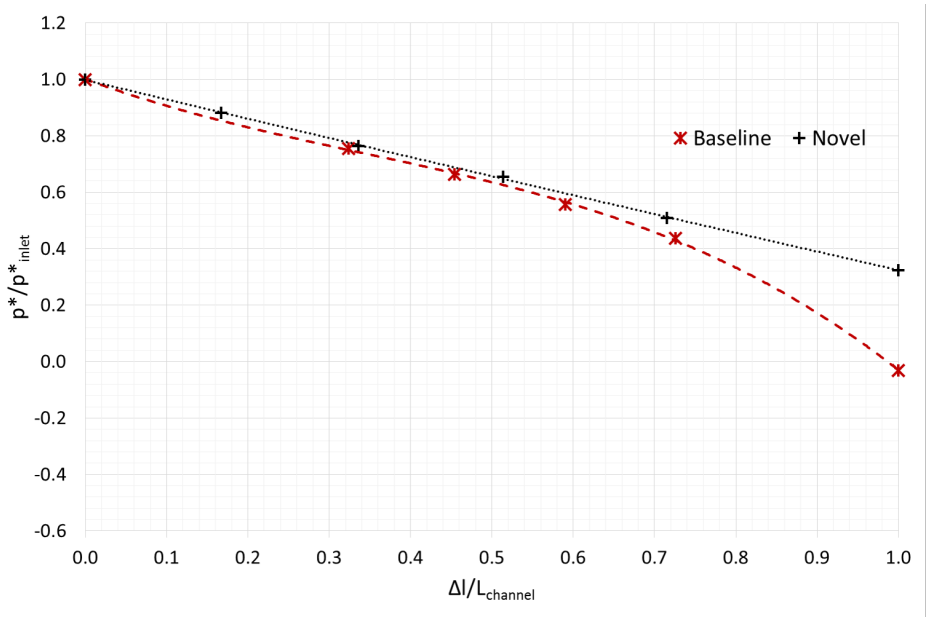

Figure 5: Trend of the rotary stagnation pressure, referred to the initial value, for the baseline and the novel geometry inside a single blade channel.

3. Numerical model

In order to verify the performance improvement prior to the construction and test of the impeller, a numerical investigation has been run with the open source code OpenFOAM by solving the 3D U-RANS equations. However, in order to validate the computational procedure, a simulation of the baseline geometry and

a comparison of the results against the consolidated ones obtained by means of the commercial CFD code CFX has been performed.

3.1. Numerical assessment

The conventional geometry has been investigated by means of numerical simulations carried out by a CFD team at Nuovo Pignone. Transient simulations have been run on a grid with 40 million cells with prism cells close to the impeller surfaces by means of the CFD commercial code ANSYS CFX ® by solving the unsteady fluid dynamic equations with a high resolution method.

The same geometry discretized by us (20 million cells and $y^+ = 30$) has been investigated with OpenFOAM by setting boundary conditions equivalent to the ones adopted in CFX. The results of the simulations for the conventional geometry are illustrated in Fig.6 and compared against the results obtained with CFX. The curves show a fairly good agreement with each other.

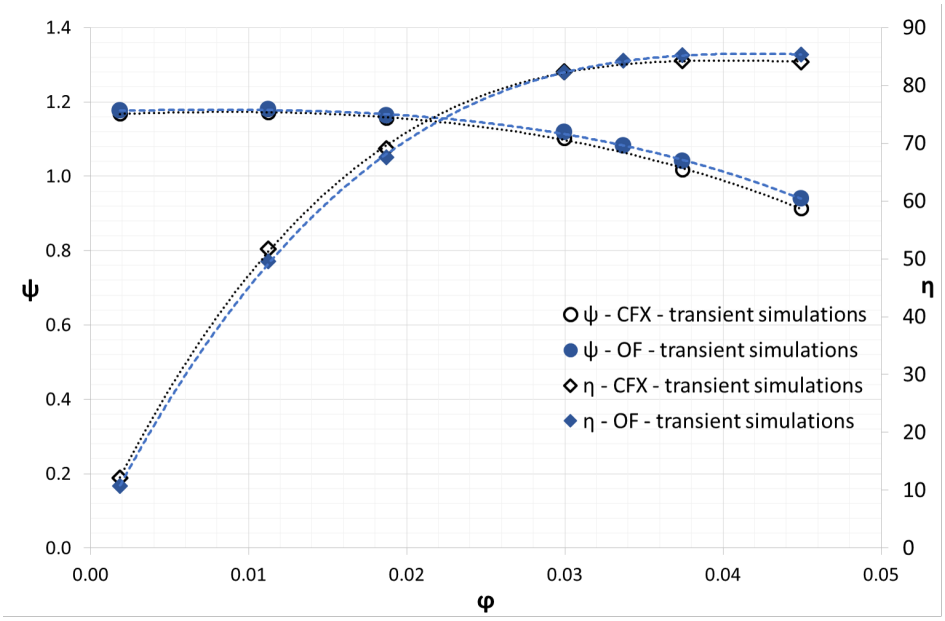

Figure 6: ψ-ϕ and η-ϕ curves calculated with CFX and OpenFOAM (Circles and rhombuses stand for ψ and η curves respectively).

3.2. Governing equations and turbulence model

The unsteady RANS equations have been considered adequate in order to model the flow through the pump [21] where quantities have to be considered averaged over a time period short enough with respect to global unsteady phenomena but long enough for statistical significance.

The turbulence model applied for the system closure is the k-ω SST as proposed by Menter [28]. This turbulence model is a standard to perform numerical analysis in hydraulic turbomachinery [29]. It automatically uses the k-ω model in the near wall region and the k-ϵ model in the regions away from the walls. The k-ω SST model can give accurate prediction of flow separation explaining its common use for the numerical investigations of flow inside centrifugal pumps.

In the OpenFOAM computational environment either steady-state or transient simulations can be run in order to study hydraulic machines, as proposed by Shah et al. [21]. For steady-state simulations the application simpleFoam can be used. This application works with incompressible, stationary flows and it is based on the SIMPLE (semi-implicit method for pressure linked equation) algorithm. Moreover, the multiple-reference-frame (MRF) technique can be employed, it actually neglects the rotor stator interaction since it does not allow the relative motion of the moving meshes (Frozen Rotor).

Because of the significant impeller-volute interaction, for the case under investigation, transient simulations have been preferred with respect to stationary ones [21]. Transient simulations in OpenFOAM involve the use of the application pimpleDyMFoam, which is based on the PIMPLE (merged PISO-SIMPLE scheme) algorithm. Rotating meshes have been considered for taking into account the impeller motion.

In the following simulations the convection, diffusion and gradient terms have been computed by using second-order upwind schemes, whereas the time derivative terms have been calculated by using a second-order backward scheme.

3.3. Numerical domain

The computational grid has been generated by means of the grid generator Icem CFD®. The grid is a hybrid mesh, see Fig.7. The volume has been discretized by means of unstructured tetrahedral elements with prism layers close to the walls in order to guarantee a wall y^+ equal to 30. The y^+ selected for this application corresponds to a correct use of the wall-functions, which involve modelling the boundary layer using a log-law distribution. Moreover, the mesh density has been increased at the leading edge of the blades and at the tongues of the volute by decreasing the value of the maximum cell dimension on these wall surfaces without changing the y^+.

Three different meshes in the *.msh* format have been generated and exported for each part of the model (namely, the suction, the impeller and the volute). Then the three *.msh* files have been converted into the OpenFOAM format with the command *fluent3DMeshToFoam* and checked with *checkMesh* routine. The entire grid is characterized by no aspect ratio problem (values < 1000 - The ratio between the longest and the shortest length), no skewness problem (values < 0.98 - Measurement of the distance between the intersection of the line connecting two cell centres with their common face and the centre of that face - smaller is better) and an orthogonality lower than $70°$ (Measurement of the angle between the line connecting two cell centers and the normal of their common face - 0.0 is the best) [30]. This avoids the use of *nonOrthogonalCorrectors* giving more accurate numerical results. Finally, the three parts have been merged together using the *mergeMesh* command.

To perform a grid refinement study three computational grids with different mesh refinement levels have been generated, see Table 2, and the results have been analyzed by means of the Grid Convergence Index (GCI) method, proposed by Roache [31]. The grids have been systematically refined with a global factor of $f_{GCI} = 1.33$. Eventually a grid made of 11 million of cells has been chosen because of small deviations in the results and a good compromise between the geometry refinement and the computational costs (see Table 2).

Table 2: Details of three computational grids, values of the hydraulic head at BEP of the centrifugal pump calculated via numerical simulations and results of the GCI method.

	Coarse	Medium	Fine	GCI_{coarse}	GCI_{fine}
Impeller (x10^6)	3	6	10		
Suction (x10^6)	1	2	4		
Volute (x10^6)	2	3	6		
Total number of elements (x10^6)	6	11	20		
Head at BEP (m)	139.8	140.8	141.0	4.87%	0.55%

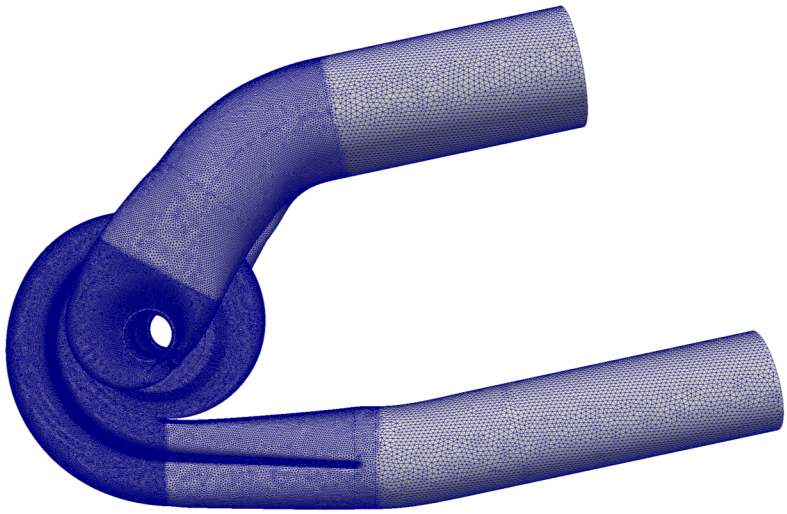

Figure 7: View of the computational domain.

3.4. Boundary conditions

For all the analyzed cases, the flow rate has been imposed at the inlet considering a uniform inlet velocity distribution. Moreover, the value of the flow leakage, which flows through the annular seal, has been modeled as exiting from the impeller case and incoming axially upstream the impeller eye with a 45° of swirl with respect to the tangential direction; it has been calculated a priori,

according to a consolidated one-dimensional empirical model, because the geometry of the seal has not been modeled [8]. A uniform pressure distribution has been imposed at the outlet of the domain. The three part of the geometry, which have been merged together, communicate each other by means of interfaces. In OpenFOAM the boundary condition used on these interfaces is named cyclicAMI (Arbitrary Mesh Interface).

Furthermore, for this test case the turbulent intensity has been assumed constant and equal to 3% at the inlet of the domain. At the inlet and outlet of the pump straight pipes have been added to reduce influence of boundary conditions.

Another critical aspect was the definition of the wall roughness in OpenFOAM; the value of the *equivalent sand grain roughness* is equal to $5.6 \cdot 10^{-5}$ m and $5.6 \cdot 10^{-6}$ m respectively for the walls of the stator and rotor parts; these values, which are the actual values of the experimental test rig, have been used for all the simulated geometries. For the purpose of activating the wall roughness, the *nutURoughWallFunction* has been applied to the walls in the *nut* file together with *kqRWallFunction* and *omegaWallFunction*, respectively for k and ω wall boundary conditions (see Tab.3). The *nutURoughWallFunction* provides a turbulent viscosity condition based on U^+ calculation and one of its argument requires the *equivalent sand grain roughness*. The *kqRWallFunction* derives from the zeroGradientFvPatchField, which means it provides Neumann boundary (the only Neumann boundary of wall functions) while *omegaWallFunction* provides the constraint on turbulence specific dissipation applying the combination of viscous and log equation.

Table 3: Summary of the boundary conditions used in OpenFOAM.

	Inlet	Outlet	Wall	Flow leakage inlet	Flow leakage out
p	zeroGradient	fixedValue	zeroGradient	zeroGradient	zeroGradient
U	massFlow	zeroGradient	fixedValue	swirlFlowRateInletVelocity	flowRateInletVelocity
k	turbulence intensity	zeroGradient	kqRwallFunction	fixedValue	fixedValue
ω	fixedValue	zeroGradient	omegaWallFunction	fixedValue	fixedValue
nut	calculated	calculated	nutURoughWallFunction	calculated	calculated

The performance of the two geometries has been evaluated at different mass flow rates. All the transient flow simulations have been carried out with a time step $\Delta t = (T/N_b)/256 = 4.5 \cdot 10^{-6}$ s where T is the time of a complete rotation and N_b the number of blades for a duration total time equal to 0.085 s, which corresponds to five complete impeller revolutions. The results in terms of head and efficiency have been averaged over the last 3 revolutions. The mean and the maximum values of the Courant number result approximately equal to 0.03 and 6, respectively, in all the simulations.

4. Experimental set up

Experimental tests have been carried out at the test rig of Nuovo Pignone (Bari, Italy). Once the prototype has been manufactured by means of a lost-foam technique, it has been tested in order to verify the performance improvement pointed out by means of the numerical simulations and to validate the entire design process. The facility is characterized by a maximum a flow rate = 600 m^3/h, a maximum pressure = 35 bar, a maximum rotational speed = 4800 rpm and a maximum electrical motor power = 200 kW. During the experimental tests the prototype absorbed at maximum 100 kW with a Reynolds number (eq.11) equal to $5 \cdot 10^6$.

$$Re = \frac{u_2 R_2}{\nu} \tag{11}$$

Data were collected at 1 s interval for a duration of 30 s, after having reached steady state conditions. The experimental setup for the characterization is constituted of a series of electronic measurement devices: two electromagnetic flow meter (accuracy 0.25%), three redundant static (accuracy 0.15%) pressure transducers either upstream and downstream the section test. A torque meter with integrated angular speed encoder characterized by an accuracy class of 0.05% is employed to calculate the hydraulic efficiency of the tested impellers. The measurement errors for Q, H, P and η at different flow rate are summurized in Fig. 8.

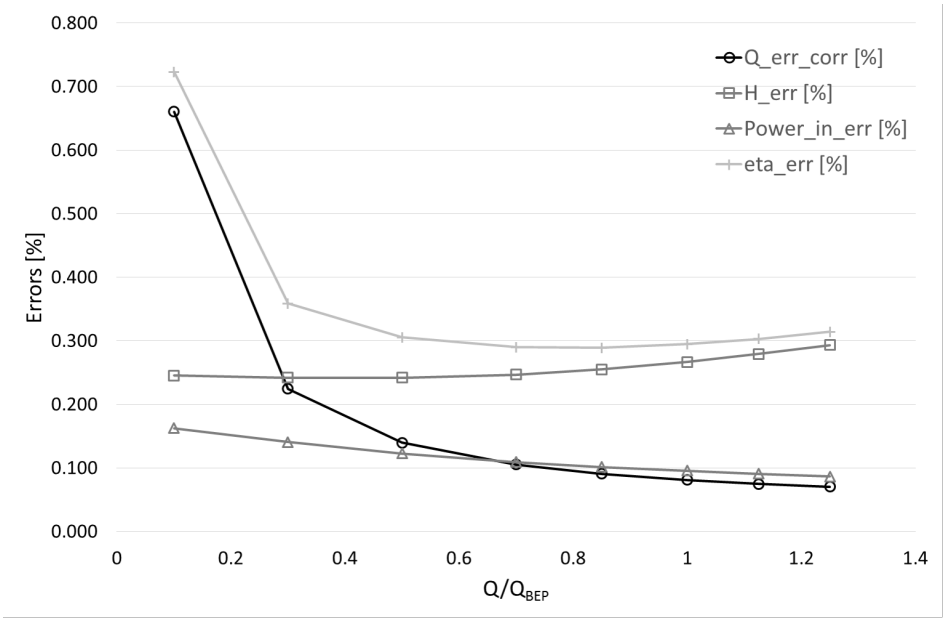

Figure 8: Description of the errors for each quantity measured at the Hydraulic test rig, Nuovo Pignone, Bari.

5. Results and discussion

As explained in the previous paragraph a campaign of simulations has been run with the purpose of simulating the entire centrifugal pump mounting the novel impeller, see Fig.9.

The numerical results have been compared against the experimental test of the novel geometry carried out in at the test rig of Nuovo Pignone (Bari, Italy) and the numerical results of the baseline calculated by means of the CFD code, CFX by a different team of Nuovo Pignone. The numerical results confirm the benefits previously pointed out by means of the single channel simulations in terms of slip factor and efficiency, see Figs. 10, 11; in fact the novel impeller shows greater values of ψ vs φ and higher global efficiency over the full range compared to the baseline geometry. Furthermore, the numerical results show a good agreement with the experimental tests.

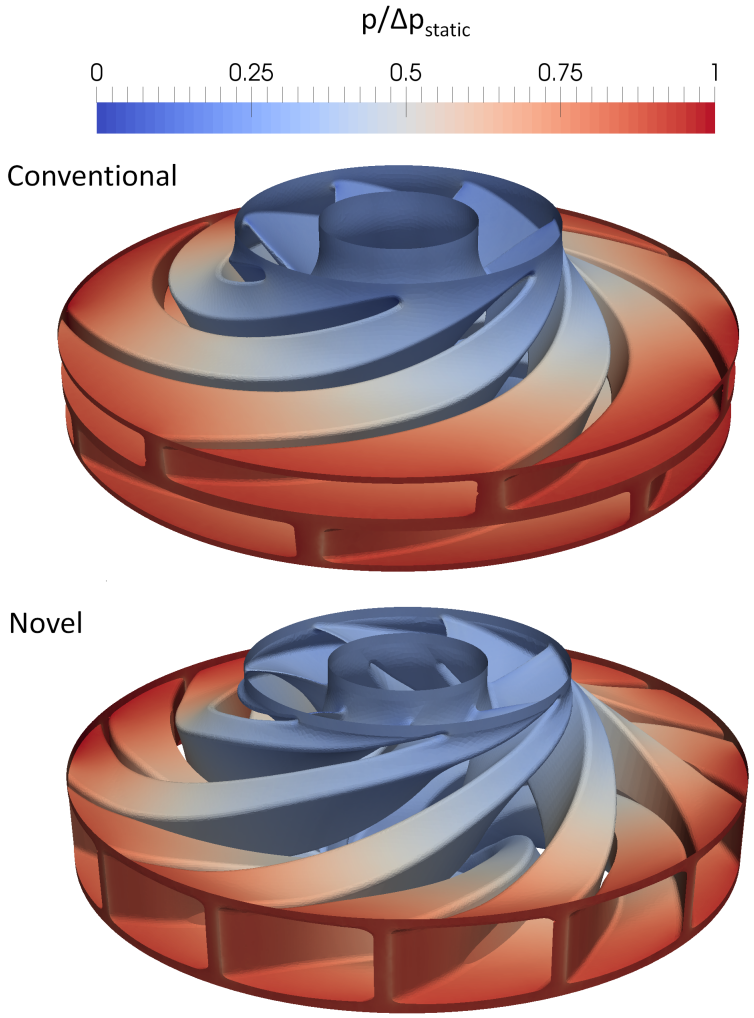

Figure 9: View of the channels designed with a conventional design tool (up) and the novel impeller for double suction centrifugal pumps covered by patent application (down).

5.1. Performance evaluation

In order to highlight the benefits from using the novel impeller, the characteristic curves of the two machines have been plotted on two non-dimensional planes. Firstly, the ψ-φ and the η-φ curves (Fig.10 - Fig.11) obtained with

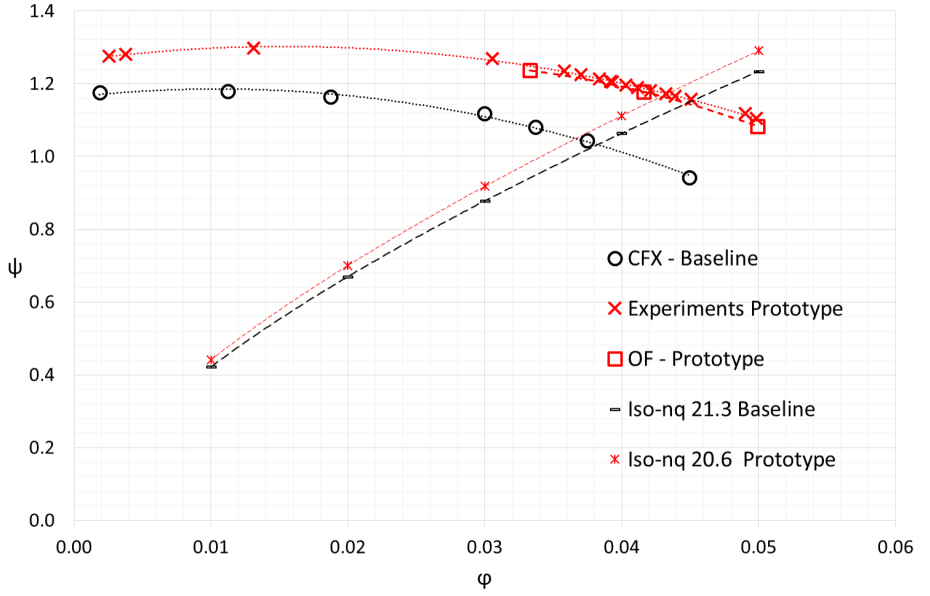

Figure 10: ψ-φ curves of the conventional impeller (CFX - Baseline) and the novel impeller obtained via numerical simulations (OF - Prototype) and experiments (Experiments Prototype); the dashed curves represent the iso-n_q which pass through the BEP of the two impellers.

OpenFOAM for the new prototype have been compared against the experimental ones and the baseline impeller performance in order to quantify the performance improvement.

In Fig.10 two iso-n_q curves, corresponding to the specific speed, n_q, of the two impellers, have been calculated according to eq.12.

$$n_q = \frac{\varphi^{1/2} cost}{\psi^{3/4}} \tag{12}$$

The specific speed is a parameter which is useful to select the right type of machine for a given application and permits a comparison of non-geometrically similar impellers. As shown in Fig.10, where two n_q iso-curves passing through the BEP of the two pumps are represented, the design process proposed for centrifugal pumps, having specific speed (n_q) comparable to the one of the baseline, is able to guarantee a relative specific speed error (n_q error) lower than

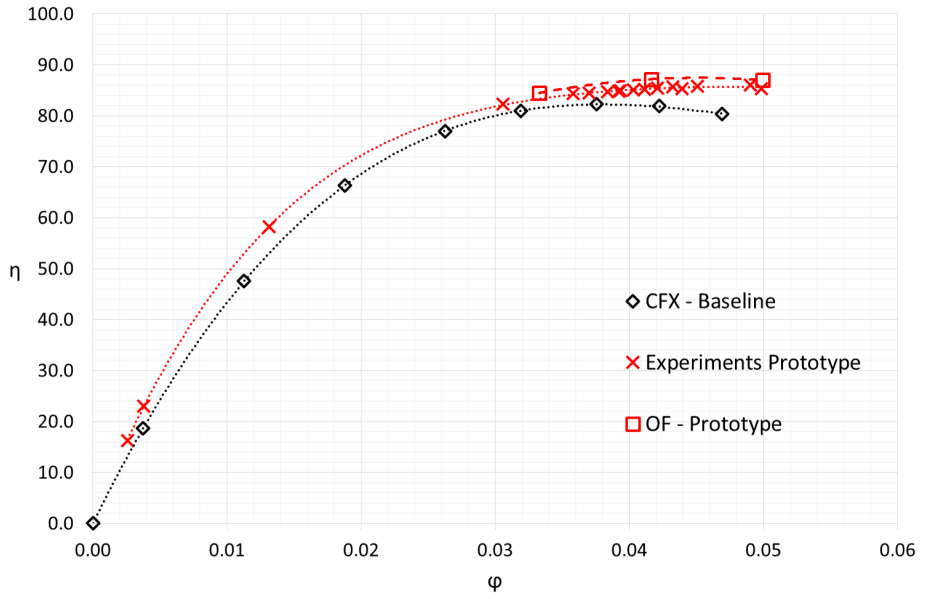

Figure 11: Efficiency curves of the conventional impeller (CFX - Baseline) and the novel impeller obtained via numerical simulations (OF - Prototype) and experiments (Experiments Prototype).

3.4 %. Therefore it is possible to make a comparison between their performance.

Considering this, it can be stated that preserving the stator parts and just substituting the baseline impeller with the novel one, the new hydraulic machine can provide a higher value of the head coefficient (see Fig.10); this means that the novel impeller is able to transfer energy to the fluid more efficiently and this substantial difference can be justified by the higher value of its slip factor, Table 1.

Another reason behind the performance improvement can be found in the enhancement of the shape and the length of the impeller channels. The cross sections of the new channels have generally larger hydraulic diameters (D_h). The new shape of the channel section, along with its reduced length, allows the reduction of the hydraulic losses ($h_{w-channel}$) inside the channels (eq.13), where ϵ is the friction factor which depends on Reynolds number and relative roughness $\epsilon = f(Re, r/D)$.

$$h_{w-channel} = \epsilon \frac{L}{D_h} \frac{w^2}{2g} \tag{13}$$

This contribution is meaningful in Fig.11 where the efficiency curves are compared. The values of the global efficiency, shown in Fig.11, are based on eq.4. This means that the shaft mechanical losses are neglected, hence:

$$\eta = \frac{\eta_g}{\eta_m} = \frac{\eta_y \eta_v \eta_m}{\eta_m} \tag{14}$$

In eq.14, η_y is the hydraulic efficiency, η_v is the volumetric efficiency and η_m is the mechanical efficiency.

The second comparison proposed is done in the $H/H_{BEP,conv}$ - $Q/Q_{BEP,conv}$ plane, where $H_{BEP,conv}$ and $Q_{BEP,conv}$ are the values of head and flow rate of the conventional geometry in correspondence of its BEP, respectively. All the curves represented in Figure 12 are scaled at the same rotational speed. In this plane are plotted: the curve obtained for the conventional geometry by means of CFD and the characteristic curves of the novel geometry, one extracted experimentally and then the same geometrically scaled in order to reach the value $H_{BEP}/H_{BEP,conv}$ and $Q_{BEP}/Q_{BEP,conv}$ equal to 1, see Fig.12.

In order to reach $H_{BEP}/H_{BEP,conv}$ and $Q_{BEP}/Q_{BEP,conv}$ equal to 1, the novel geometry needs a size reduction equal to 5.5%, applied along all the three coordinates (x, y, z). This means that the novel impeller would lead to a machine smaller than the conventional one and consequently to a reduction of the industrial cost and occupied volume.

5.2. Flow analysis at the outlet of the impellers

A study of both the velocity (Figs.13, 14) and the vorticity (Fig.18) fields at the outlet of the impeller has been carried out with the aim to further investigate the benefits of the novel configuration. A comparison between the two geometries has been done in order to evaluate the fluid characteristics in the region between the impeller outlet and the volute inlet and to understand how the flow field is influenced by the new design of the novel impeller.

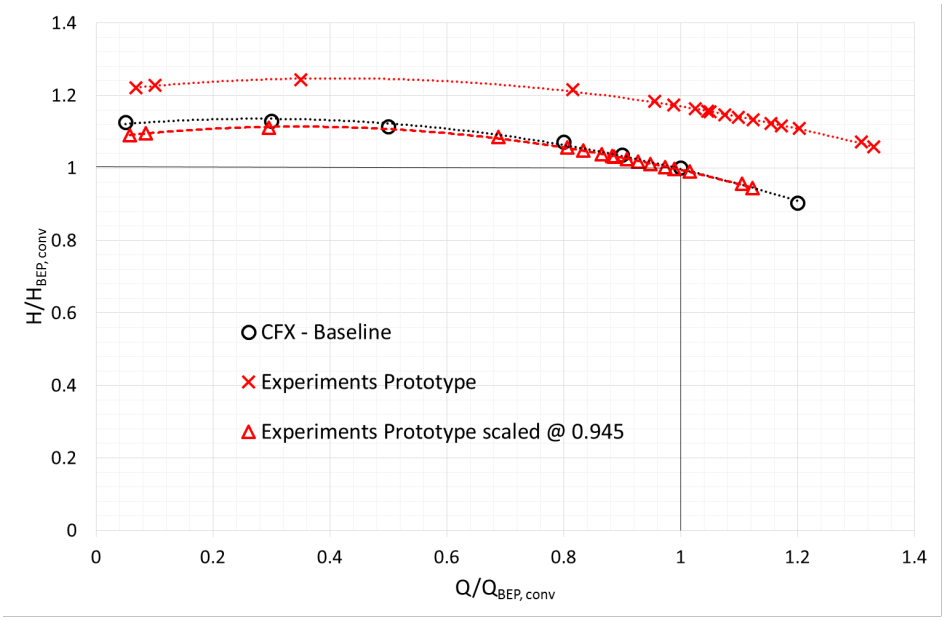

Figure 12: Comparison of the characteristic curves between the conventional geometry (CFX - Baseline), the novel geometry (Experiments Prototype) and the novel geometry scaled to reach $H_{BEP}/H_{BEP,conv}$ and $Q_{BEP}/Q_{BEP,conv}$ equal to 1.

5.2.1. Velocity profiles

Figure 13 shows the contours of the dimensionless velocity magnitude (c_2/u_2) at the outlet of the two impellers; the velocity contours at the outlet of the novel impeller configuration are particularly more homogeneous than in the traditional one. Indeed, the standard deviation of the velocities along the axial direction is equal to 0.68 and 0.45 for the conventional and the novel impeller, respectively (Fig.14).

It is well known that a square duct limits the secondary flows compared to a rectangular one, hence velocity unbalances between the corners of cross section are reduced. This means a reduction of the secondary losses and a better flow guidance [8]. Velocity profiles have been calculated on surfaces at the outlet of the impeller along the axial direction averaged over 360°. These are reported in Fig.14 and point out that the velocity profile at the outlet of the novel impeller

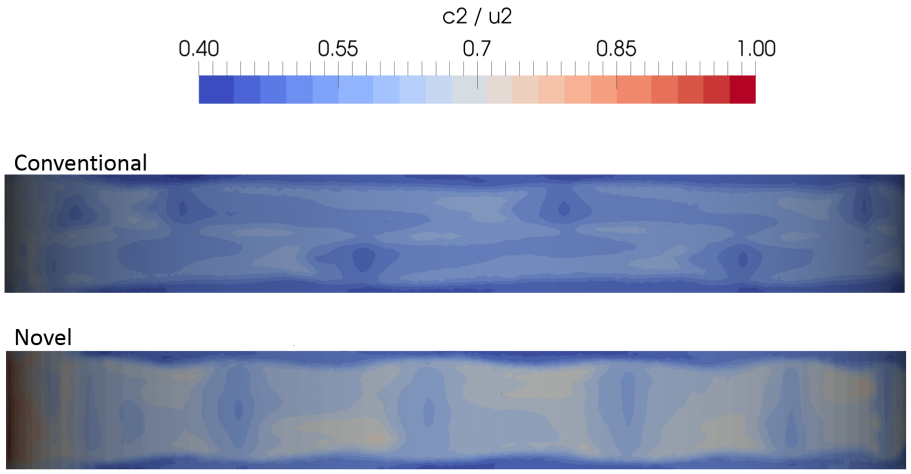

Figure 13: Contours of the dimensionless velocity magnitude c_2/u_2 at the outlet of the conventional (up) and novel geometry (down).

follows a flatter profile on the other hand the baseline shows a velocity ripple in the middle, therefore the division element (i.e., the round plate between the two single suction centrifugal pumps in back-to-back configuration) influences the mixing flow in the baseline configuration. Moreover, the theoretical values of the absolute velocity magnitude (c_2) calculated at the outlet of the impellers are represented in Fig.14. It can be stated that the velocity profile at the outlet of the novel geometry is closer to the target value, calculated by means of the congruent blade theory, compared to the baseline geometry. The relative errors between the mean velocities calculated by means of CFD and the theoretical velocities for the novel and the baseline are equal to 4.8% and 9.6%, respectively.

Moreover, the velocity profile have been plotted along the circumferential direction over 360° by cutting a cylindrical surface between the impeller outlet and volute inlet with three planes, see Fig.15. The first plane is at the half of the impeller (middle plane), the other two are at different axial distance ($\pm l_2/2$, where l_2 is the blade height at the outer diameter) with respect to the middle one. The results (Fig.16 and 17) are averaged over the last 5 rotations of the machine.

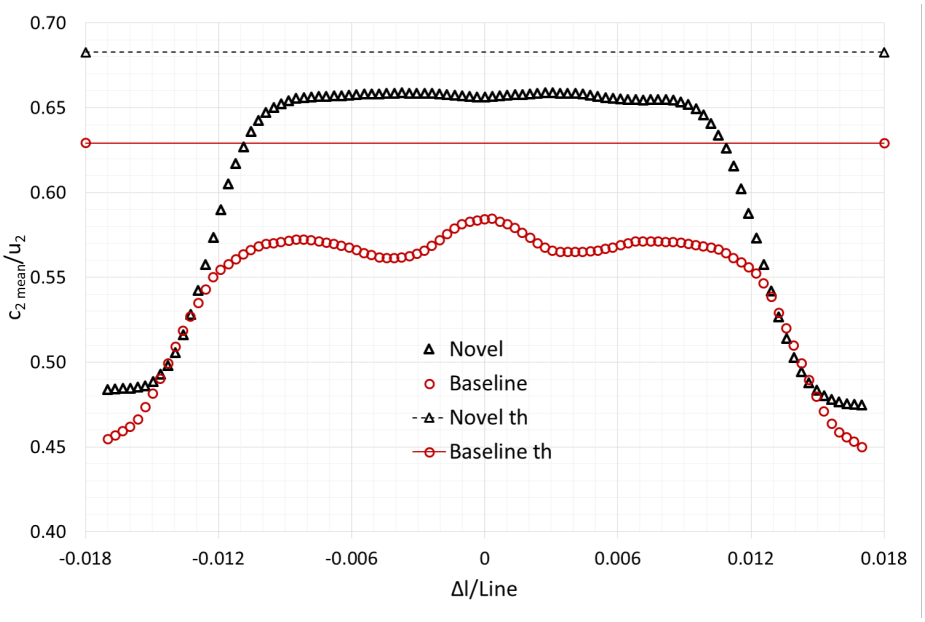

Figure 14: Averaged velocity profiles at the outlet of the traditional and new geometry along the axial direction, where u_2 is the tangential velocity at the outer diameter.

The baseline configuration shows a velocity profile with a frequency equal to $2N_b f_{rotation}$ on the middle plane; on the other hand, the velocity profiles of the two back-to-back impellers display saw-tooth evolutions with $f = N_b f_{rotation}$, see Fig.17. The novel impeller has low velocity oscillations (relative to the mean value) except that close to the trailing edge of the blades where the velocity increases. The velocity peaks coincide with the suction side of the impeller. The analysis of the velocity points out a different behavior in correspondence of the middle plane; the novel impeller displays a smooth oscillation of the velocity, whereas the baseline presents oscillations higher than those at the half of the vanes' exits.

5.2.2. Vorticity field

A study of the vorticity field points out that the vorticous structures that develop between the left and right side of the baseline impeller vanish when the novel geometry is employed, see Fig.18. Furthermore, iso-surfaces of the Q-

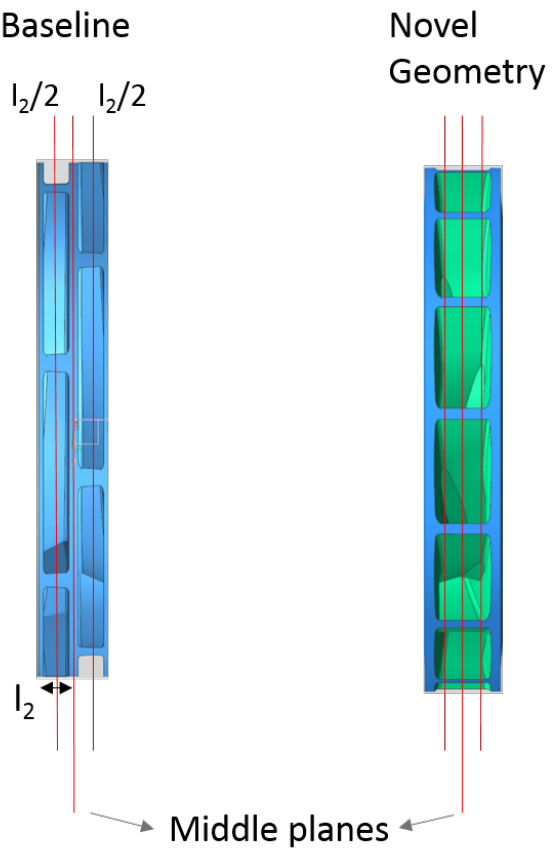

Figure 15: View of the impeller outlet with three planes on which velocity and pressure have been calculated.

criterion vortex [32] are shown in Fig.19. These iso-surfaces describe the wake structures. In the conventional geometry these are due to the presence of the division element between the two impellers in back-to-back configuration, see Fig.19,a. On the other hand, only vertical structures remain as in the conventional geometry in correspondence of the leading edge of the blades. Thus, the novel configuration might help the flow guidance and the reduction of the secondary flows, which develop inside the volute, diminishing the losses inside of it. The absence of the division element allows a better flow mixing between the two side of the impeller, indeed the velocity ripple is suppressed. It is well

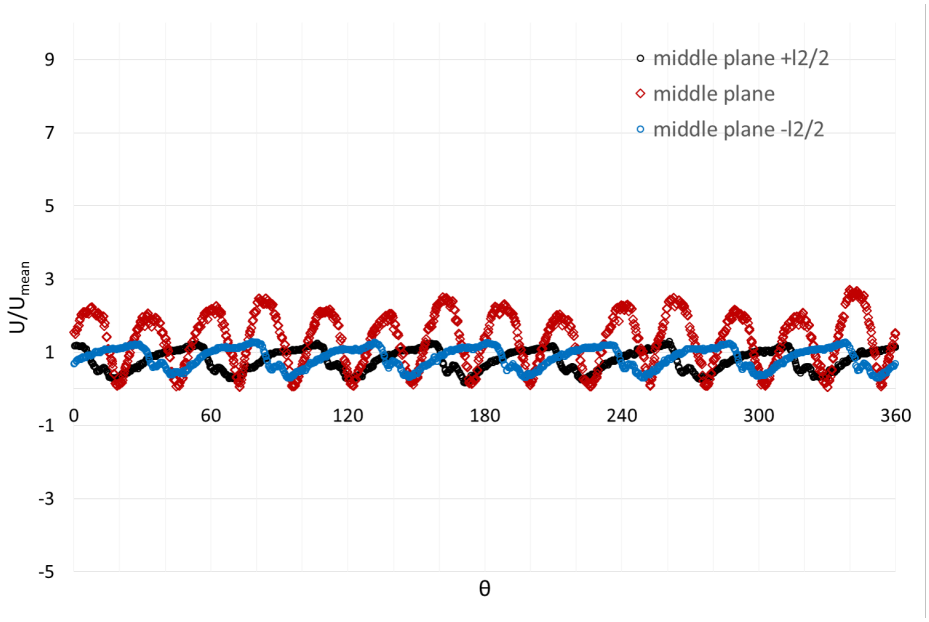

Figure 16: Averaged velocity profiles at the outlet of the baseline impeller.

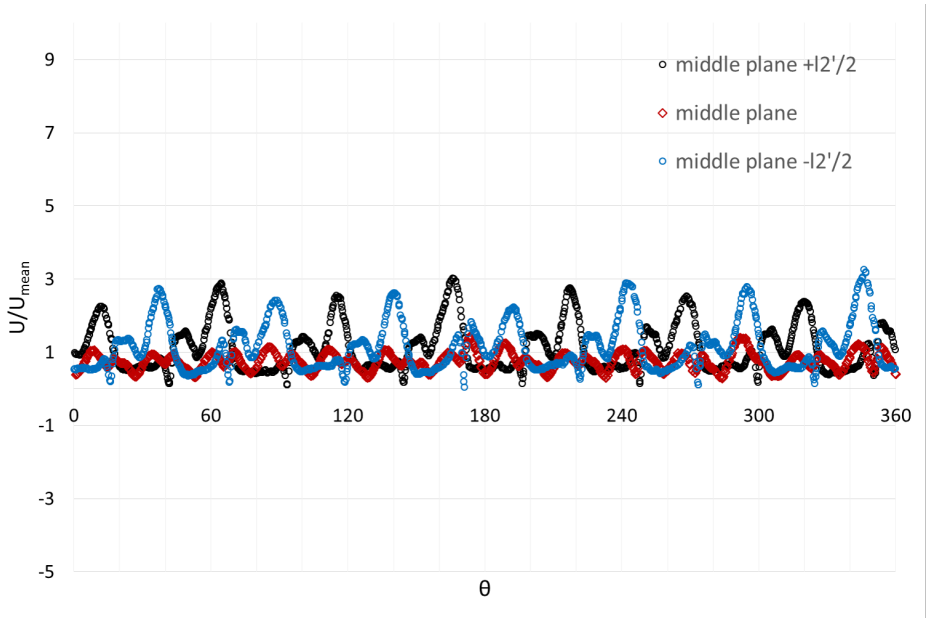

Figure 17: Averaged velocity profiles at the outlet of the novel impeller.

known that inside the volute secondary flows develop and the flow pattern has the shape of a double vortex. This secondary flow becomes increasingly asymmetrical with growing non-uniformity of the impeller outflow (see velocity ripple Fig.14 and velocity profile in correspondence of the middle planes of the two geometries Fig.16 and 17).

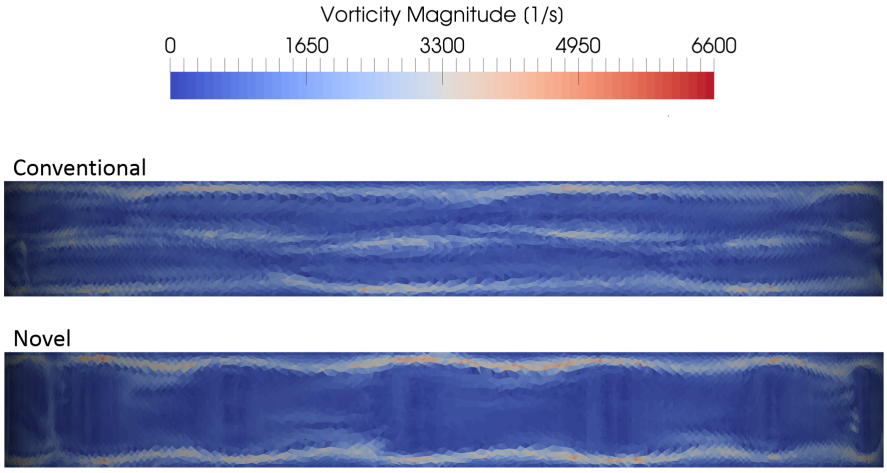

Figure 18: Contours of the vorticity field at the outlet of the traditional (up) and novel geometry (down).

5.3. Analysis of the pressure fluctuations

Pressure pulsations and head evolution have been studied to investigate possible drawback of the novel geometry. Contrary to the velocity trends, the pressure profile of the baseline shows a saw-tooth trend in the middle plane, with a $2N_b f_{rotation}$. On the other hand, the novel geometry displays a pressure profile identical for each position of the planes. Even if the baseline impeller tends to smooth the pressure peaks and valleys due to the arrangement of the two single suction impellers, it shows locally higher pressure amplitude than the novel impeller (4.38% and 3.75%, respectively).

Moreover, the head, calculated via numerical simulations has been studied in order to further investigate pressure fluctuations inside the volute. This gives

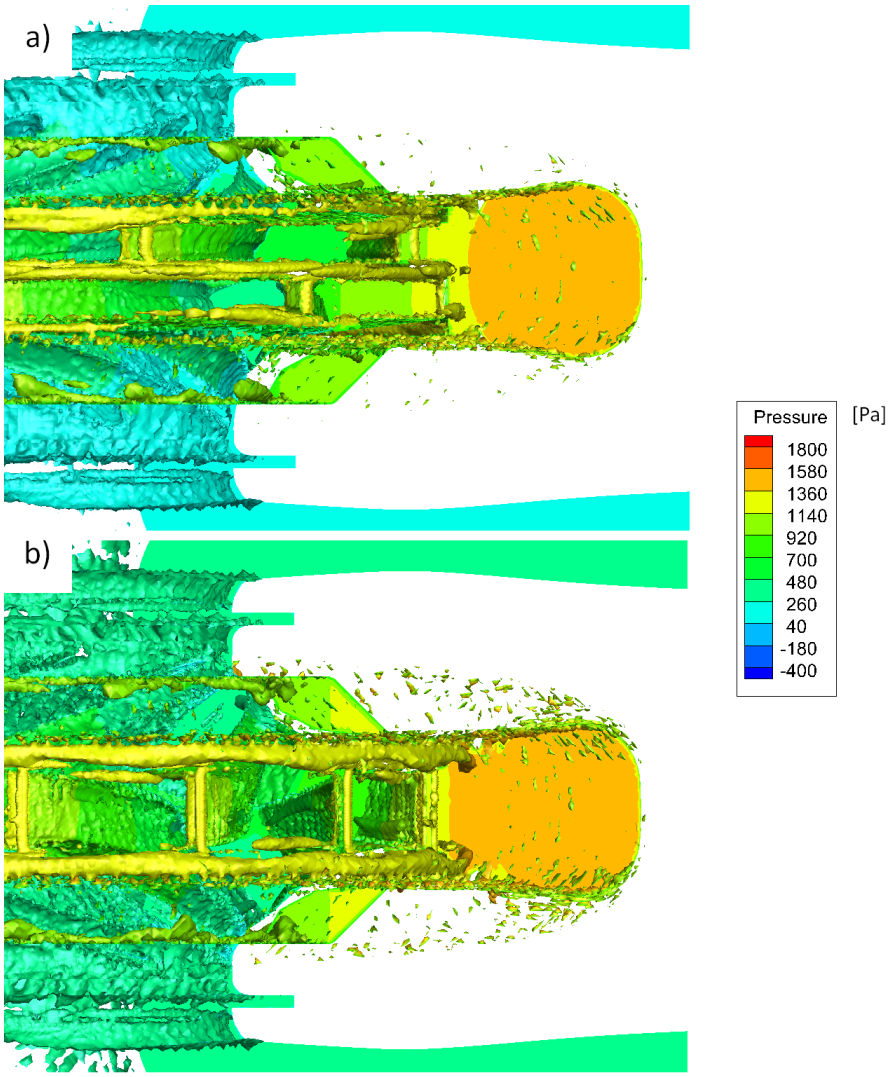

Figure 19: Iso-surfaces of the vortex criterion Q colored by pressure contours of the static pressure of the baseline (a) and the novel geometry (b).

indications about the dynamic interaction between the blades and the tongues of the double volute. The evolution of the head over an interval corresponding to the time necessary to complete a 1/7 of a complete rotation, namely equal to $360°/N_b$, has been plotted in Fig.22. The frequencies of the two curves are equal to $2N_b f_{rotation}$, whereas the novel geometry shows a higher pressure fluctuation,

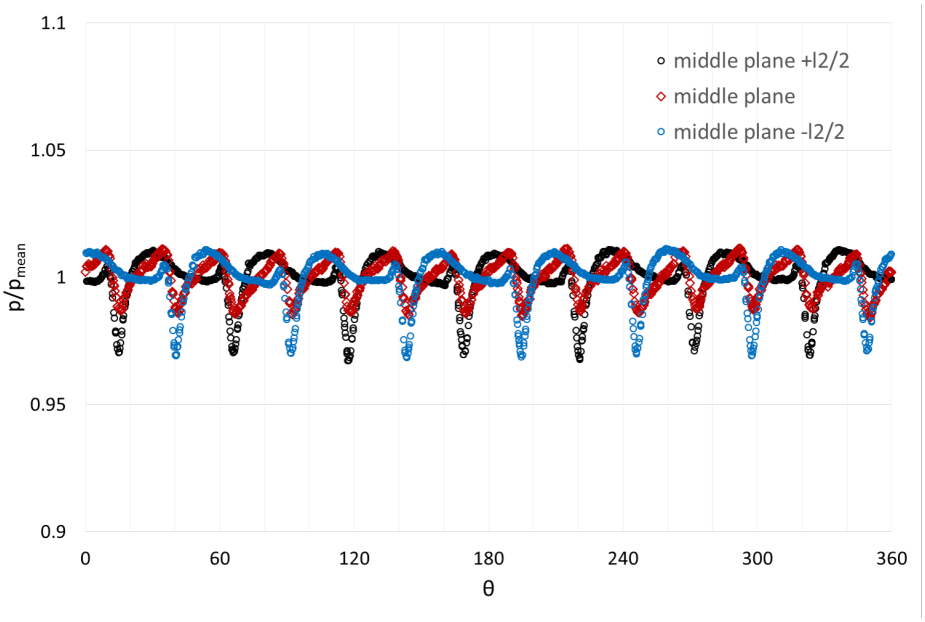

Figure 20: Averaged pressure profiles at the outlet of the baseline impeller.

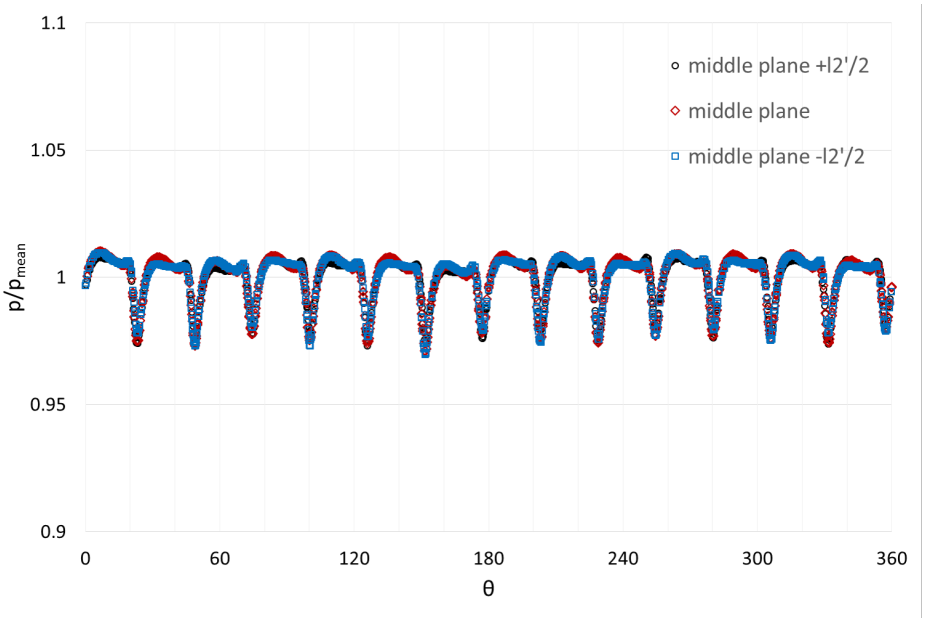

Figure 21: Averaged pressure profiles at the outlet of the novel impeller.

i.e., the values of the relative standard deviation of the head (σ_{Head}/H_{mean}) are 2.29% and 3.71% for the baseline and the novel impeller, respectively. Indeed, both values can be generally accepted. This result confirms what pressure profiles highlight along the circumferential direction, namely the arrangement of the baseline geometry is prone to cut pressure peaks.

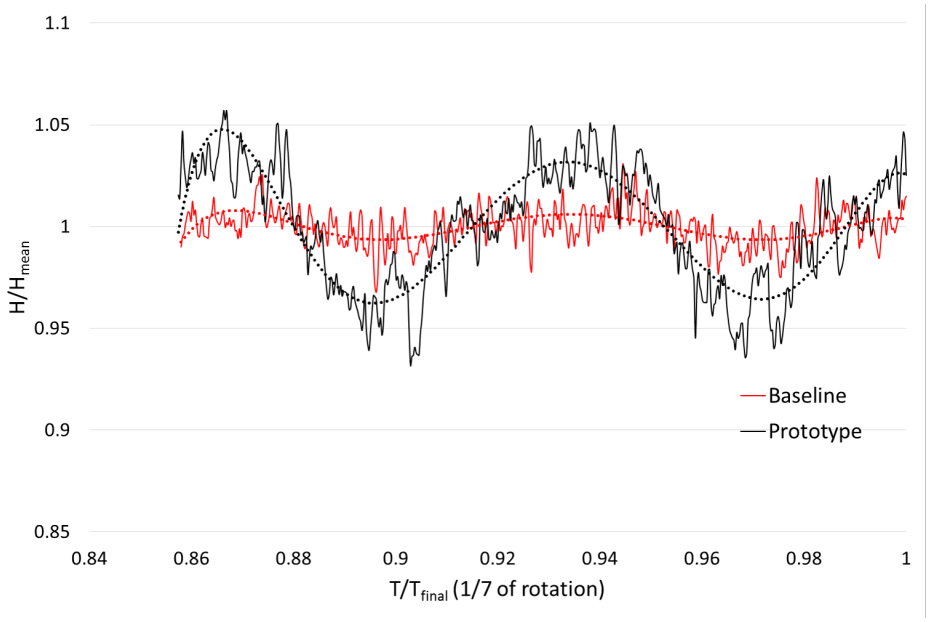

Figure 22: Averaged head (H) evolution over pressure value over a time equal to $(T/T_{final})/N_b = 1/7$ of a complete rotation.

A higher amplitude could drive the piping system to oscillate with greater amplitude at specific frequencies if the frequencies of the pulsations are equal to the system's resonant frequencies.

It is worth to highlight that the novel impeller has been designed with the aim to reduce slip phenomena and not to obtain lower pressure pulsations than the baseline. Nevertheless, if necessary, pressure fluctuations of the novel geometry can be reduced by changing blade trailing edge inclination, see Fig.23, [8]. This allows one to distribute forces on a longer surface. Typically, λ_{La} can vary from 70 to 90°. Moreover, in case the frequency coincides with that of the

piping system, to avoid resonance frequencies at least three parameters can be changed: the number of blades of the impeller, the system's resonant frequencies and the rotational speed.

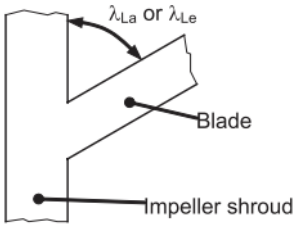

Figure 23: Blade inclination (λ_{La}) with respect to the impeller shroud.

5.4. Impact of the novel technology on carbon footprint

According to the results shown in this paper, it can be stated that the introduction of this technology, instead of the conventional one, can allow a reduction of the energy consumption in energy power plants, namely a reduction of the electric motor energy. Besides, it allows a reduction of the volume occupied and the installation of hydraulic turbomachinery with higher power density. Narrowing it down to a nuclear power plant, we can consider, for instance, the China's Hualong One. This plant has three primary coolant loops with pumps driven by 6.6 MW electric motors each (110 t each pump set). Its gross energy production is 1170 MWe and the energy consumed by the pumps is equal to 19.8 MW. Under the hypothesis that the conventional and the novel geometry have the same weight, a size reduction of 5.5% can be applied to provide the same pressure rise of a baseline. Furthermore, considering the price of stainless steel = 1200 $euro/t$ a money saving of the 28000 euro (-15.6%) on the cost of the pumps can be reached by substituting the three conventional geometry with novel ones. In terms of efficiency the retrofit of the conventional geometries could lead to energy saving over the global energy consumption equal to 0.198 MW, which corresponds to a reduction of CO_2 emission equal to 99 t_{CO_2}.

6. Conclusions

In this work a novel impeller, that can easily retrofit a conventional one, for a low-medium specific speed double suction centrifugal pump has been presented. Considering that double suction centrifugal pumps are the main devices involved in the feedwater system of nuclear power plants and that they are responsible for a significant share of their energy consumption (by affecting the balance of both the gross and net electrical energy production), the obtained efficiency increase, even if of only a few percentage points, is a substantial result in the economy of these power plants.

This new geometry has been designed respecting the following geometric and fluid dynamic constraints: to have the same specific speed number (n_q) of the baseline geometry; to guarantee a kinematic flow angle at the inlet of the volute (α_3) in accordance with the optimum α_3 of the volute and to satisfy the matching with the absolute inlet flow angle at the outlet of the inlet duct.

Firstly, a 1D code has been written to design the novel impeller and numerical simulations of a single blade vane have been run by means of a commercial code and by solving 3D steady state RANS equations in order to evaluate the hydraulic losses and the slip factor. These values have been then passed back to the 1D code until convergence is reached. Once the final geometry has been chosen, the entire geometry of the centrifugal pump has been studied via numerical simulations to take into account the interaction of the novel impeller and the stator parts. The computational fluid dynamics analysis has been performed with an open-source code named OpenFOAM by solving 3D U-RANS with the k-ω SST model for turbulence closure.

The numerical simulations and the experimental tests display an impeller which is able to transfer more efficiently energy to the fluid compared to the baseline having higher value of the slip factor. Moreover, the novel design of the channel provides a higher efficiency over the full range and a slight reduction of the fluid flow rotary stagnation pressure inside of it. This means that a more efficient machine can be installed preserving the same dimensions of the baseline (higher

pressure rise) or alternatively the adoption of the new geometry can lead to a size reduction (volume, weight and cost) when the same head of the baseline is required and it allows to assemble a more compact system than the ones currently used.

Furthermore, the velocity and vorticity contours at the outlet of the impeller show an impeller that is able to provide a better flow guidance and a more homogeneous fluid flow at the inlet of the volute. This is accompanied by slightly higher pressure fluctuations which can be reduced, if required, by increasing the trailing edge inclination. The averaged velocity profiles at the outlet of the impeller and the wake structures evaluated by means of the vorticity criterion Q highlight the benefits from the absence of the division element with the novel impeller.

The gain in pump efficiency could significantly contribute to industrial energy saving. For instance, by retrofitting the three pumps of the Hualong One nuclear power plant an energy saving equal to 0.198 MW can be reached. This corresponds to a CO_2 emission reduction of 99 tCO_2.

In future works an impeller with reduced number of blades, i.e, higher hydraulic blade loading, will be designed to explore its performance and the efficiency of the new geometry and to correlate the number of blades with the slip factor value for the novel design.

Eventually simulations of the geometry studied in this work as a turbine are suggested since the blade arrangement and the new channel design are thought to be adequate to improve the fluid guidance under PaT (pump as turbine) operating mode.

References

[1] U.s. energy information administration. international energy outlook 2017 (2017).
URL `https://www.eia.gov/outlooks/ieo/`

[2] B. C. Waide P, Energy-efficiency policy opportunities for electric motor-driven systems international energy agency energy efficiency series.

[3] V. K. A. Shankar, S. Umashankar, S. Paramasivam, N. Hanigovszki, A comprehensive review on energy efficiency enhancement initiatives in centrifugal pumping system, Applied Energy 181 (2016) 495 – 513. doi:https://doi.org/10.1016/j.apenergy.2016.08.070.
URL http://www.sciencedirect.com/science/article/pii/S0306261916311576

[4] T. Sahoo, A. Guharoy, Energy cost savings with centrifugal pumps, World Pumps 2009 (510) (2009) 35 – 37. doi:https://doi.org/10.1016/S0262-1762(09)70104-X.
URL http://www.sciencedirect.com/science/article/pii/S026217620970104X

[5] Nuclear power reactors (2018).
URL http://www.world-nuclear.org/information-library/nuclear-fuel-cycle/nuclear-power-reactors/nuclear-power-reactors.aspx

[6] Z. Zou, F. Wang, Z. Yao, R. Tao, R. Xiao, H. Li, Impeller radial force evolution in a large double-suction centrifugal pump during startup at the shut-off condition, Nuclear Engineering and Design 310 (2016) 410 – 417. doi:https://doi.org/10.1016/j.nucengdes.2016.10.034.
URL http://www.sciencedirect.com/science/article/pii/S0029549316304125

[7] Study on improving the energy efficiency of pumps, European Commission, 2001.

[8] J. F. Gulich, Centrifugal pumps, 2nd Edition, 2006. doi:10.1007/978-3-642-40114-5.

[9] J. Skrzypacz, M. Bieganowski, The influence of micro grooves on the parameters of the centrifugal pump impeller, International Journal of Mechanical Sciencesdoi:https://doi.org/10.1016/j.ijmecsci.2017.01.039.
URL http://www.sciencedirect.com/science/article/pii/S002074031730200X

[10] Y. Zhang, S. Hu, J. Wu, Y. Zhang, L. Chen, Modeling and multi-objective optimization of double suction centrifugal pump based on kriging metamodels, in: D. Gao, N. Ruan, W. Xing (Eds.), Advances in Global Optimization, Springer International Publishing, Cham, 2015, pp. 251–261.

[11] S. Derakhshan, M. Pourmahdavi, E. Abdolahnejad, A. Reihani, A. Ojaghi, Numerical shape optimization of a centrifugal pump impeller using artificial bee colony algorithm, Computers & Fluids 81 (2013) 145–151. doi:10.1016/j.compfluid.2013.04.018.
URL http://linkinghub.elsevier.com/retrieve/pii/S0045793013001588

[12] D. V. L. d'Agostino, A. Pasini, A reduced order model for preliminary design and performance prediction of tapered inducers: Comparison with numerical simulations.

[13] C. Wang, W. Shi, X. Wang, X. Jiang, Y. Yang, W. Li, L. Zhou, Optimal design of multistage centrifugal pump based on the combined energy loss model and computational fluid dynamics, Applied Energy 187 (2017) 10 – 26. doi:https://doi.org/10.1016/j.apenergy.2016.11.046.
URL http://www.sciencedirect.com/science/article/pii/S0306261916316324

[14] T. Schaefer, M. Neumann, A. Bieberle, U. Hampel, Experimental investigations on a common centrifugal pump operating under gas entrainment conditions, Nuclear Engineering and Design 316 (2017) 1 – 8. doi:https://doi.org/10.1016/j.nucengdes.2017.02.035.

URL http://www.sciencedirect.com/science/article/pii/S0029549317301024

[15] Patent - gb18343 (1900).

[16] Patent - jp2012132368 (2012).

[17] Patent - us1003542 (1911).

[18] Patent - us2791183.

[19] K. ltd Patent JPS58155298A, Impeller for double suction pump (1983).

[20] Patent - jph0687694u (1994).

[21] S. Shah, S. Jain, R. Patel, V. Lakhera, Cfd for centrifugal pumps: A review of the state-of-the-art, Procedia Engineering 51 (2013) 715 – 720. doi:http://dx.doi.org/10.1016/j.proeng.2013.01.102.

[22] H. Nilsson, Evaluation of openfoam for cfd of turbulent flow in water turbines, 23rd IAHR Symposiumdoi:http://dx.doi.org/10.1016/j.proeng.2013.01.102.
URL http://www.sciencedirect.com/science/article/pii/S1877705813001033

[23] B. Kye, K. Park, H. Choi, M. Lee, J.-H. Kim, Flow characteristics in a volute-type centrifugal pump using large eddy simulation, International Journal of Heat and Fluid Flow 72 (2018) 52 – 60. doi:https://doi.org/10.1016/j.ijheatfluidflow.2018.04.016.
URL http://www.sciencedirect.com/science/article/pii/S0142727X17311797

[24] R. Mittal, G. Iaccarino, Immersed boundary methods, Annual Review of Fluid Mechanics 37 (2005) 239–261, cited By 1483. doi:10.1146/annurev.fluid.37.061903.175743.
URL https://www.scopus.com/inward/record.uri?eid=2-s2.

0-14544293952&doi=10.1146%2fannurev.fluid.37.061903.175743&
partnerID=40&md5=6a7851b7facee1a728943ead3f6d2e5c

[25] A. Posa, A. Lippolis, R. Verzicco, E. Balaras, Large-eddy simulations in mixed-flow pumps using an immersed-boundary method, Computers & Fluids 47 (1) (2011) 33 – 43. doi:https://doi.org/10.1016/j.compfluid.2011.02.004.
URL http://www.sciencedirect.com/science/article/pii/S0045793011000569

[26] M. Specklin, Y. Delaur, A versatile immersed boundary method for pump design, Pump Users International Forum, September, 2016.

[27] High efficiency double suction impeller - patent application - 20180128271 (2017).

[28] F. R. Menter, Two-equation eddy-viscosity turbulence models for engineering applications, American Institute of Aeronautics and Astronautics.

[29] P. H. J. Bardina, T. Coakley, Turbulence modeling validation, testing, and development, NASA Technical Memorandum, vol. 110446.

[30] Openfoam - checkmesh (2015).
URL http://openfoamwiki.net/index.php/CheckMesh

[31] P. J. Roache, Perspective: A method for uniform reporting of grid refinement studies, Journal of Fluids Engineering 116(3):405 (1994) 405–413. doi:10.1115/1.2910291.

[32] G. Haller, An objective definition of a vortex, Journal of Fluid Mechanics 525 (2005) 126. doi:10.1017/S0022112004002526.